ACS APPLIED MATERIALS & INTERFACES

Research Article

www.acsami.org

Simple Additive-Free Method to Manganese Monoxide Mesocrystals and Their Template Application for the Synthesis of Carbon and Graphitic Hollow Octahedrons

Mingtao Zheng, Yingliang Liu,* Yong Xiao, Hanwu Dong, Haobin Feng, Haoran Zhang, and Bingfu Lei

Department of Applied Chemistry, College of Science, South China Agricultural University, Guangzhou 510642, China

Supporting Information

ABSTRACT: Mesocrystals are of great importance owing to their novel hierarchical microstructures and potential applications. In the present work, a simple additive-free method has been developed for the controllable synthesis of manganese monoxide (MnO) mesocrystals, in which cheap manganese acetate ($Mn(Ac)_2$) and ethanol were used as raw materials without involving any other expensive additives such as surfactants, polyelectrolyte, or polymers. The particle size of the resulting MnO mesocrystals is tunable in the range 400−1500 nm by simply altering the concentration of $Mn(Ac)_2$ in ethanol. The percentage yield of the octahedral MnO mesocrystals is about 38 wt % with respect to the starting $Mn(Ac)_2$. The selective adsorption of oligomers, which was resulted from the polymerization of ethanol, acted as an important role for the mesocrystal formation. A mechanism involving the oriented aggregation of MnO nanoparticle subunits and the subsequent ripening process was proposed. Moreover, for the first time, the as-synthesized MnO mesocrystals were employed as a novel template to fabricate functional materials with an octahedral morphology including MnO@C core/shells, carbon, and graphitic hollow octahedrons. This method shows the importance of mesocrystals not only for the field of material research but also for the application in functional materials synthesis.

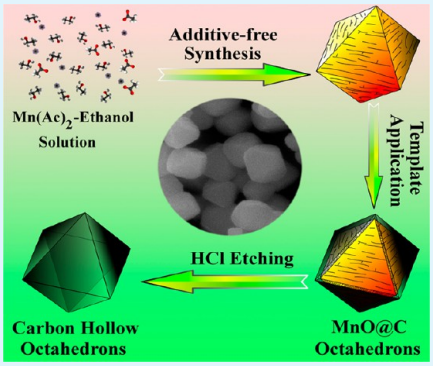

KEYWORDS: *mesocrystals, manganese monoxide, carbon hollow octahedrons, controllable synthesis, template application*

1. INTRODUCTION

Micro/nanomaterials have attracted great interest owing to potential applications in adsorption, separation, catalysis, energy, sensors, nanoelectronic devices, biotechnology, and other areas.[1−6] Recently, extensive efforts have been devoted to the self-assembly of nanoparticles (NPs) into highly ordered one-, two-, and three-dimensional architectures or superstructures because of their importance in basic research and potential applications.[7−12] Particularly, mesocrystals, which are a new class of nanostructured solid materials, have attracted rapidly increasing interest since they were first proposed by Cölfen and Antonietti in 2005.[13] Mesocrystals usually have a much higher crystallinity than polycrystalline materials and, in some cases, exhibit the properties of single crystals. Therefore, mesocrystals have a high potential for many applications, such as catalysis, sensing, energy storage and conversion, separation, optical storage, and drug delivery.[14−20]

To date, a large number of advanced techniques have been developed to fabricate various mesocrystals, such as $CaCO_3$,[21−23] $BaCO_3$,[24] $BaSO_4$,[25] $CoPt_3$,[26] copper oxalate,[27] metal oxides,[28−35] etc. However, in the most of these studies, to get a mesocrystal with well-ordered morphology, the complex and expensive organic additives, such as polyelectrolyte,[36−38] surfactants,[39−43] polymers,[44−50] etc. as a crystal growth modifier or template are often involved. The synthesis of mesocrystals in a simple solution system has rarely been demonstrated.[51,52] Moreover, the control over the shape and size of mesocrystals was difficult. Nevertheless, the mechanism for mesocrystal synthesis is still poorly understood. Although more and more mesocrystal systems have been synthesized, the new physical and chemical properties arising from the mesocrystal structure need to be revealed and their potential application as functional materials is still far from being exploited. Hence, establishing an efficient, simple, and low-cost synthesis method for preparation of mesocrystals with controllable size would be of great benefit to their large-scale production and practical applications.

In the present work, we report a simple additive-free way to prepare cubic MnO mesocrystals with an octahedron morphology and tunable size. This method is based on the reduction of manganese acetate ($Mn(Ac)_2$) and ethanol in a sealed autoclave system. The particle size of the well-ordered mesocrystals can be tuned from 500 to 1500 nm by simply varying the concentration of $Mn(Ac)_2$ solution in ethanol. Remarkably, the as-synthesized MnO mesocrystals were employed, for the first time, as a novel template to fabricate MnO@C core/shells, carbon, and graphitic hollow octahedrons with controllable particle sizes. This method may provide an

Received: September 8, 2013
Accepted: November 25, 2013
Published: November 25, 2013

   dx.doi.org/10.1021/am403875p | ACS Appl. Mater. Interfaces 2013, 5, 12561−12570

alternative to "classic" methods for the synthesis of metal oxides, mesocrystals, and carbon hollow structures with specific morphologies.

2. EXPERIMENTAL SECTION

2.1. Preparation of Well-Ordered MnO Mesocrystals. All reagents were used as purchased without further treatment. In a typical process, 1.0 g of manganese acetate ($Mn(Ac)_2$) was dissolved in 40 g of ethanol under magnetic stirring. Then the obtained solution was put into a stainless steel autoclave with a 60 mL capacity, which was sealed and then placed into an electric furnace. The temperature of the furnace was increased to 400 °C in 30 min and maintained at 400 °C for 12 h. After the solution cooled to room temperature naturally, the jade-green precipitates were collected and washed with absolute ethanol and distilled water for several times. The obtained products were then dried in a vacuum at 60 °C for 6 h. Finally, about 0.38 g of reseda power was obtained. The percentage yield of MnO was about 95 wt % with respect to the theoretical yield (the theoretical output is about 0.40 g) and 38 wt % with respect to the $Mn(Ac)_2$ starting material.

2.2. Preparation of MnO@C Core/Shell Structures, Carbon, and Graphitic Hollow Octahedrons. The precipitates prepared through the above process and 10 mL of ethanol were placed into a stainless steel autoclave with a 40 mL capacity. The autoclave was sealed and then placed into an electric furnace. The temperature of the furnace was increased to 600 °C in 60 min and maintained at 600 °C for 6 h. After the solution cooled to room temperature naturally, the black powder was collected. To prepare graphitic hollow octahedrons, the unwashed MnO mesocrystals were calcined at 900 °C for 6 h under nitrogen atmosphere in tubular furnace. All the obtained black powders were washed with absolute ethanol and distilled water for several times. To further prepare carbon hollow octahedrons, the obtained black powder was dipped in dilute HCl(aq) (~0.1 mol·L^{-1}) for 3 h under magnetic stirring and then washed with distilled water for several times. All the obtained products were then dried in a vacuum at 60 °C for 6 h.

2.3. Characterization. X-ray diffraction (XRD) patterns were recorded on an MSAL-XD2 X-ray diffractometer with Cu Kα radiation (36 kV, 20 mA, λ = 1.5406 Å). Fourier transform infrared (FTIR) spectra were measured by an Equinox 55 (Bruker) spectrometer with the KBr pellet technique ranging from 500 to 4000 cm^{-1}. Morphologies and microstructures of the samples were characterized by field-emission scanning electron microscopy (FESEM), transmission electron microscopy (TEM), and high-resolution TEM (HRTEM). The SEM measurements were taken with a Philips XL-30 and JSM 6300F scanning electron microscopes. TEM images and chemical elements of the products were obtained using a JEOL JEM-2010 transmission electron microscope with an operating voltage of 200 kV. The specific surface areas were determined from nitrogen adsorption using the Brunauer–Emmett–Teller (BET) equation. The total pore volume was determined from the amount of gas adsorbed at the relative pressure of 0.99. Pore size distribution was derived from the analysis of the adsorption branch using the Barrett–Joyner–Halenda (BJH) method.

3. RESULTS AND DISCUSSION

3.1. Characterization of MnO Mesocrystals. Figure 1 shows FESEM images of the five representative samples synthesized by the present additive-free approach, which are assigned as MOM-500, MOM-600, MOM-750, MOM-900, and MOM-1500) (MOM denotes manganese monoxide mesocrystals, the number gives the mean particle size in nanometers). Low resolution SEM images (Figure S1, Supporting Information) also reveal that all the samples have the relatively uniform octahedron morphology in large domains. As shown in Figure 1a, the sample MOM-500 prepared at a low $Mn(Ac)_2$/ethanol ratio of 1:40 contains uniform octahedrons that are

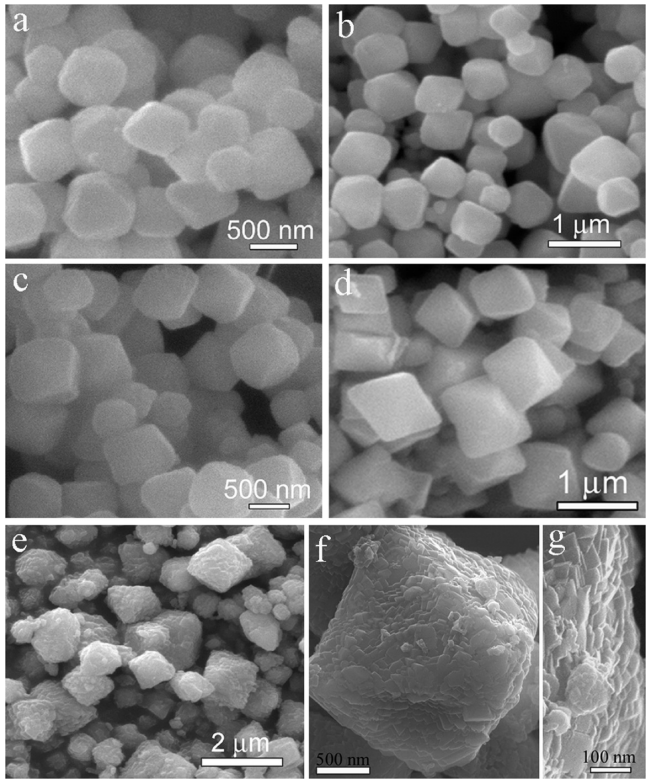

Figure 1. SEM images of the well-ordered MnO mesocrystals with different particle sizes: (a) MOM-500, 500 nm; (b) MOM-600, 600 nm; (c) MOM-750, 750 nm; (d) MOM-900, 900 nm; (e–g) MOM-1500, 1500 nm. The mass ratio between $Mn(Ac)_2$ and ethanol are 1:40, 1:20, 1:15, 1:10, and 1:5, respectively.

separated from each other. The sizes of the octahedrons typically range from 400 to 600 nm, with an average edge length of approximately 500 nm. It can be observed that the mean particle size of the MnO mesocrystals increases from 500 to 1500 nm as the mass ratio of $Mn(Ac)_2$/ethanol increases from 1:40 to 1:5 (Figure 1a–e). Figure 1f shows the top view of one MnO octahedron, from which one can see that the octahedron consists of four triangular faces and one rectangular base with a mean edge length of 1500 nm. It is worth noting that the rough surface and some NPs with sizes of 40–50 nm can be observed for the sample MOM-1500 (Figure 1e–g), suggesting the MnO octahedral mesocrystals are resulted from self-assembling of MnO NP subunits rather than the classic crystal growth.

Figure 2 presents the corresponding TEM images of the MOM samples with different particle sizes. Figure 2a shows the sample of MOM-500 has a uniform tetragonal projected shape, consistent with the octahedron morphologies observed by SEM. The edge lengths of the isolated octahedrons are approximately 500 nm, which corresponds well with the FESEM results. A typical TEM image of the boundary of a single mesocrystal, further confirms that the MOM-500 consists of nanosized subunits with sizes of around 30–40 nm (Figure 2a1). It may be noted that a large amount of nanopores with sizes of around 3–4 nm can be observed inside the particle for the MOM-500 (Figure 2a2), supporting the formation of nanoporous mesocrystals. This result was further confirmed by the N_2 adsorption/desorption measurement, which indicated the presence of rather uniform nanopores with an average diameter of 3.8 nm (Figure S2, Supporting Information). The

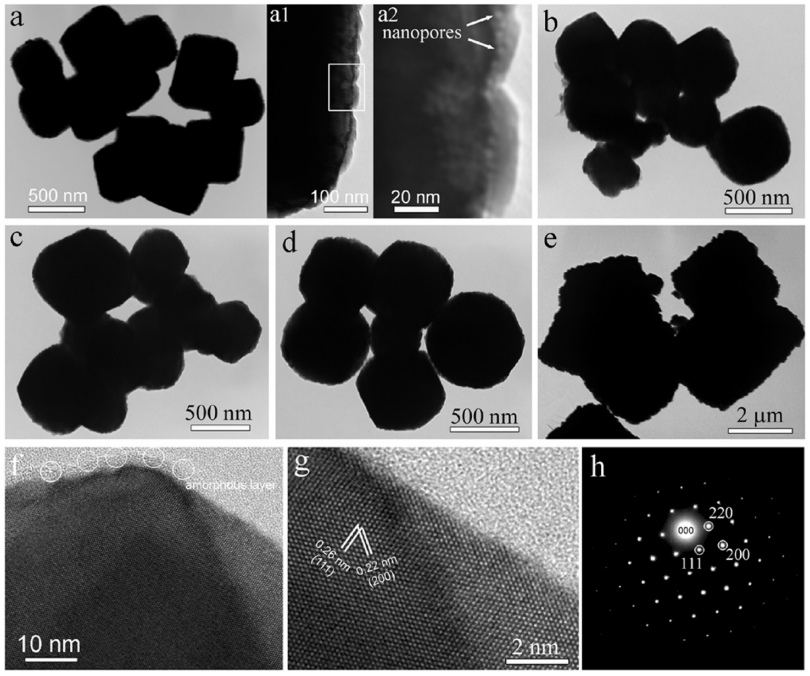

Figure 2. TEM images of the well-ordered MOMs with different particle sizes: (a) MOM-500, 500 nm; (b) MOM-600, 600 nm; (c) MOM-750, 750 nm; (d) MOM-900, 900 nm; (e) MOM-1500, 1500 nm. (f, g) HRTEM images and (h) corresponding SAED pattern of the sample MOM-500.

BET surface area and the pore volume were determined to be 158 $m^2\ g^{-1}$ and 0.23 $m^3\ g^{-1}$, respectively. Figure 2b–e shows the typical TEM images of MOM-600, MOM-750, MOM-900, and MOM-1500, suggesting that the particle size of MnO mesocrystals increases with increasing the concentration of $Mn(Ac)_2$ in ethanol. These results indicate that the particle size of the MnO mesocrystals can be controlled by simply varying the concentration of $Mn(Ac)_2$ solution in ethanol.

The microstructure of the MnO mesocrystals was further characterized by HRTEM measurement (Figures 2f–h). The well-resolved lattice fringes give interplanar spacing of 0.26 and 0.22 nm, in good agreement with the distances of the (111) and (200) planes, respectively, of cubic MnO (Figure 2g). The corresponding selected area electron diffraction (SAED) pattern (Figure 2h) evidently reveals the single-crystalline nature of the MnO octahedrons. It is worth noting that a thin amorphous layer with a thickness of around 3–4 nm can be observed (indicated by white rings in Figure 2f), which may be resulted from the selective adsorption of certain oligomers formed by polymerization of organic species.[53]

3.2. Formation Mechanism of the MnO Mesocrystals. To shed light on the formation mechanism of the MOMs, their growth process was followed by examining the products harvested at different intervals of reaction time. The precipitates obtained at different reaction times without calcination were characterized by electron microscopy, XRD, and FTIR. The phase identification of the synthesized samples was carried by XRD analysis. In a short reaction time, the ethanol-assisted thermolysis of $Mn(Ac)_2$ results in the formation of manganese carbonate ($MnCO_3$). For instance, the precipitates formed after 3 h of reaction at 400 °C are pure rhomb-centered $MnCO_3$ (JCPDS no. 86-0173, Figure 3a). When the reaction time increases to 6 h, the resultant $MnCO_3$ begins to be decomposed into MnO. It is worth noting that, at this stage, the decomposition reaction of $MnCO_3$ was uncompleted, and thus the coexistence of MnO and $MnCO_3$ can be observed in

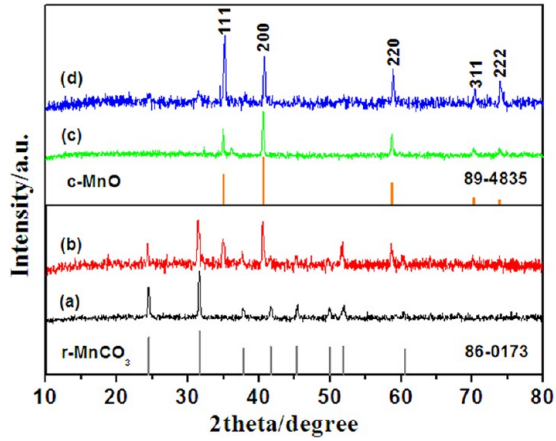

Figure 3. XRD patterns of the samples obtained by the reaction of 1.0 g of $Mn(Ac)_2$ in 40 g of ethanol at a temperature of 400 °C for different reaction times: (a) 3 h, (b) 6 h, (c) 12 h, and (d) 24 h.

the sample (Figure 3b). When the reaction time is prolonged to 12 h, the product is composed of phase-pure MnO, indicating the complete decomposition of $MnCO_3$ in the long reaction time. As shown in Figure 3c, the XRD pattern of the sample MOM-500 displays the following diffraction peaks (2θ[deg]): 34.96, 40.62, 58.75, 70.21, and 73.84, which can be correlated to the (*hkl*) indices (111), (200), (220), (311), and (222), respectively, indicating the formation of face-centered cubic MnO (JCPDS PDF no. 89-4835). It is worth noting that the diffraction intensity of (111) plane increases with even longer reaction time, indicating the selective growth of MnO crystalline in this process (Figure 3d).

Corresponding to the above phase evolution, the morphologies of the obtained samples are presented in Figure 4. In a short reaction time of 3 h, $MnCO_3$ NPs with size of around 30–40 nm can be obtained (Figure 4a–c). It is well known that the self-assembly and mesoscale transformation can produce

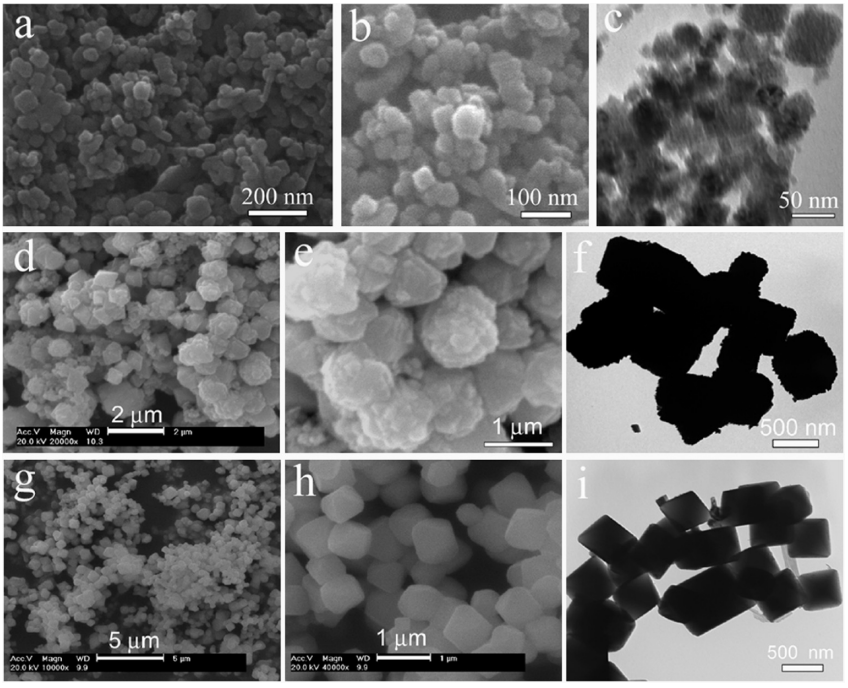

Figure 4. SEM and TEM images of the samples obtained by solvothermal reaction of 1.0 g of $Mn(Ac)_2$ in 40 g of ethanol at a temperature of 400 °C for different reaction times: (a–c) 3 h, (d–f) 6 h, and (g–i) 24h.

mesocrystals with controlled structures and morphologies.[54,55] In the present case, with the increase of reaction time, the NPs are self-assembled into larger aggregates with quasi-polyhedral morphologies (Figure 4d–f). Meanwhile, $MnCO_3$ begins to decompose into MnO crystals when the reaction time is increased to 12 h, and pure-phased MnO mesostructures with an octahedron morphology can be obtained (Figure 1). The ripening or fusion of these MnO NP subunits results in the formation of MnO octahedrons with smoother surfaces when the reaction time is further prolonged to 24 h (Figure 4 g–i). From the HRTEM images shown in Figure S3 (Supporting Information), a thin amorphous layer with thickness of about 3–4 nm can be observed clearly, also indicating the presence of oligomers on the surface of the mesocrystals.

The presence of the oligomers can be further confirmed by FTIR spectroscopy of the corresponding samples (Figure 5). It reveals that a strong characteristic peak at 3440 cm^{-1} is attributed to the O—H bending vibration, which implies the existence of hydroxyl groups. The absorption peak at 1090 cm^{-1} corresponds to the C—OH stretching and OH bending vibrations, and the peaks at 2927 and 2850 cm^{-1} originate from the C—H stretching vibration. The bands at around 1636 cm^{-1} can be attributed to C=C vibrations, suggesting the aromatization of ethanol; whereas other bands in the 1000–1450 cm^{-1} range correspond to C—O (hydroxyl, ester, or ether) stretching and O—H bending vibrations. As denoted by ■, two peaks at around 626 and 518 cm^{-1} arise from the stretching vibration of the Mn—O and Mn—O—Mn bonds.[56–58] The vibration bands for C—O stretching that are normally observed at 1463.4 and 875.7 cm^{-1} for CO_3^{2-} shift down to 1433 and 862 cm^{-1}, respectively (denoted by ●). This shift maybe results from the vibration motion of CO_3^{2-}, which is restricted by the surface adsorption of organic groups such as hydroxyl and carboxyl, similarly to the results in our previous work.[53] These results indicate that there is a large number of oligomers with hydroxyl and carboxyl groups on the surfaces of MOMs, which is in good agreement with HRTEM observations. As the reaction time is increased, ethanol is transformed into organic species, such as ethers, esters, or other oligomers. It is worth noting that the transformation including dehydration and polymerization of ethanol is complicated, and the component of the resulted organic species is very complex. Although it is difficult to determine the component of these organic species accurately, it can be believed that the coordination between these organic species and $MnCO_3$ and MnO NPs was prerequisite for MnO octahedron formation.

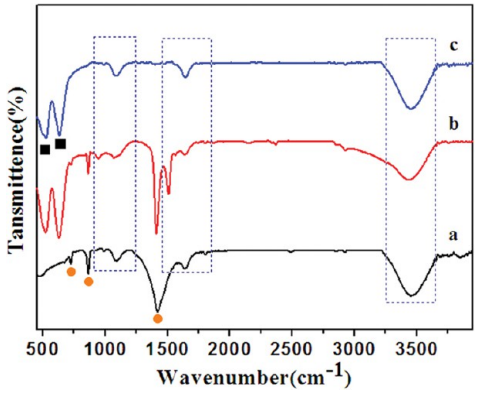

Figure 5. FTIR spectra of the samples obtained by the reaction of 1.0 g of $Mn(Ac)_2$ in 40 g of ethanol at a temperature of 400 °C for different reaction times: (a) 3 h, (b) 6 h, and (c) 12 h.

On the basis of the above time-dependent transformation process, the formation mechanism of MnO octahedral mesocrystals and their shape evolution can be illustrated in detail in Scheme 1. Firstly, a large number of $MnCO_3$ nanocrystallites nucleate and grow into small NPs in the initial stage. The obtained $MnCO_3$ is decomposed into MnO owing to the high temperature with the increase of the reaction time.

Scheme 1. Schematic Illustration of the Formation Mechanism and the Shape-Evolution Processes of the Octahedral MOMs

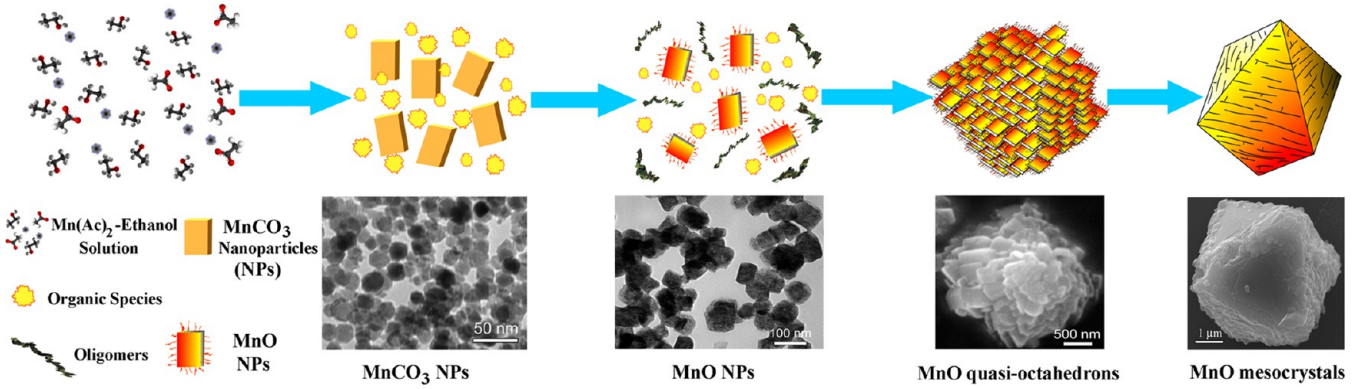

Meanwhile, the polymerization of ethanol and other organic species results in the formation of certain oligomers, which can be absorbed selectively onto the surfaces of $MnCO_3$ and MnO nanocrystals confining their growth into large crystals. To minimize the overall energy of the system, these small NPs tend to aggregate together to form MnO quasi-polyhedrons.[59,60] Subsequently, the quasi-polyhedral aggregates change into octahedrons due to the ripening mechanism. Therefore, MnO octahedral mesocrystals are obtained through the synergic effect of oriented attachment and ripening mechanism.

To further prove this formation mechanism, a control experiment was conducted in which the $MnCO_3$ NPs produced without ethanol were employed for the subsequent growth in solution containing a certain amount of ethanol at 400 °C. Figure 6 shows the TEM images of the small $MnCO_3$ NPs with

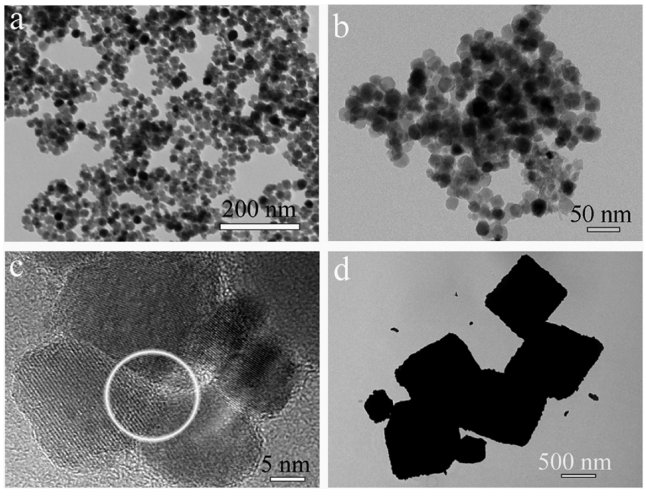

Figure 6. (a) TEM image of $MnCO_3$ small NPs prepared using distilled water instead of ethanol at 400 °C for 3 h. (b and c) TEM and HRTEM images of $MnCO_3$ NPs after solvothermal treatment in ethanol at 400 °C for 3 h, the annulus in (c) showing one of the areas where the NPs have already been oriented and aggregated with each other. (d) TEM image of MnO mesocrystals prepared by solvothermal treatment of $MnCO_3$ NPs in ethanol at 400 °C for 12 h.

size of 20−30 nm using distilled water instead of ethanol with other experimental conditions kept the same. It can be seen that when $MnCO_3$ NPs were solvothermal treated in ethanol at 400 °C for 3 h, the small NPs have already had the tendency to be oriented-attached and aggregated with each other (Figure 6b,c). When the reaction time was increased to 12 h, MnO octahedral mesocrystal composed of small NPs and with size of about 1400 nm were formed (Figure 6d). It is worth noting that the oriented attachment process is dynamically slow in the present case, because the polymerization of ethanol is a very slow process. It can be concluded that the formation process of the MnO mesocrystals involves two consecutive stages. At the initial stage, an oriented attachment process is dominating, whereas at the subsequent stage, a ripening process dominates. The initial oriented attachment process is critical to this kind of formation process based on the slow polymerization of ethanol and subsequent selective-adsorption of resulted oligomers, which is different to the reported Cu_2O microcrystals using oleic acid as selective adsorption additive.[61]

On the basis of the above results, it is reasonable to reason that the present strategy based on the oriented attachment and ripening mechanism provides a simple, cost-effective way to synthesize MnO mesocrystals with an octahedral morphology by using $Mn(Ac)_2$ and ethanol as starting materials. It is worth noting that this method can also be employed to synthesize other metal oxide mesocrystals with polyhedral morphologies. For example, nickel monoxide polyhedral mesocrystals could also be prepared by using nickel acetate instead of $Mn(AC)_2$ while keeping other experimental parameters consistent (Figure S4, Supporting Information). The inset in Figure S4 (Supporting Information) shows the magnified SEM image of one single mesocrystal, clearly showing that the mesocrystal consists of a large number of nickel monoxide NPs. These results indicate that the present work will provide a general way toward rational fabrication of various kinds of metal oxide mesocrystals.

3.3. Characterization of MnO@C Core/Shell Structures. It has been demonstrated that the drawbacks resulting from surface-absorbed surfactants were the unpredictable influence on the toxicity of the NPs and the diminished accessibility of the particle surface.[62−64] However, the removal of organic additives after synthesis is still challenging to date, though it may alter the surface chemistry unfavorably for certain applications. In the present work, an amorphous layer with thickness of about 3−4 nm can be observed clearly on the surface of the mesocrystals, even though they have been washed by distilled water and ethanol for several times, as shown in Figures 2 and S3 (Supporting Information). Fortunately, these MnO mesocrystals with adsorbed oligomers were employed as starting materials to fabricate MnO@C core/shell structures, for the first time, which is then subjected to an HCl etching process resulting in the formation of carbon hollow octahedrons (CHOs) with controllable sizes.

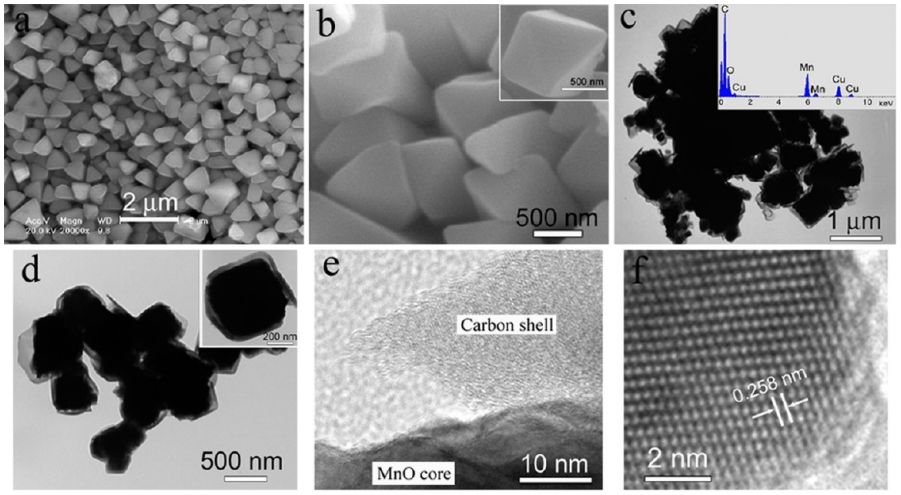

Figure 7. (a, b) SEM, (c, d) TEM, and (e, f) HRTEM images of the obtained MnO@C core/shell octahedrons using MOM-600 as starting material. Inset in c shows the corresponding EDS spectrum. Carbonization conditions: 600 °C, 6 h.

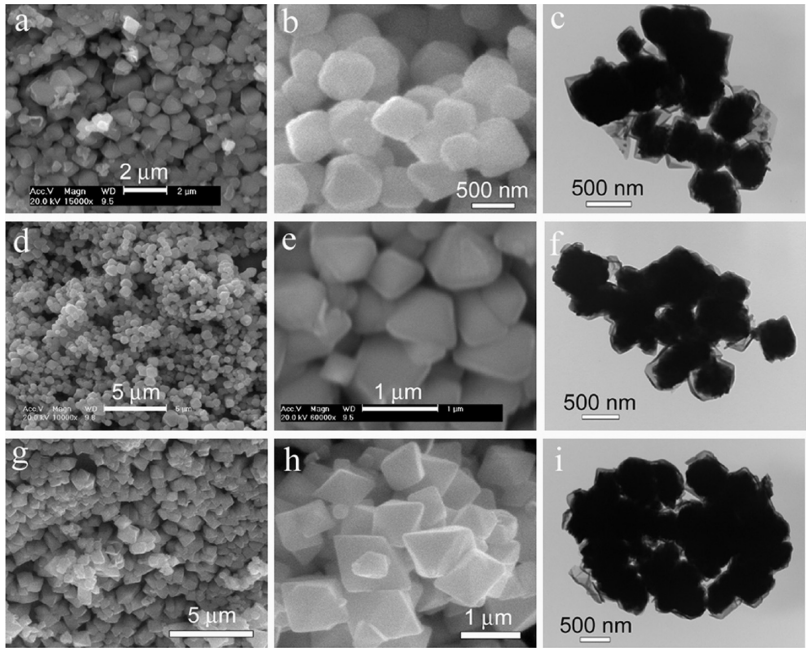

Figure 8. SEM and TEM images of the synthesized MnO@C core/shell octahedrons using different MOM samples as starting materials: (a–c) MOM-500, (d–f) MOM-750, and (g–i) MOM-900. Carbonization conditions: 600 °C, 6h.

When calcined at a higher temperature, the absorbed oligomers will be carbonized in situ onto the surfaces of the MOMs, resulting in the formation of MnO@C core/shell octahedrons. As shown in the SEM images (Figure 7a,b), these core/shell structures present relatively perfect octahedral morphologies (Figure 7b inset), of which the edge length is about 600–800 nm. From the TEM images in Figures 7c,d, the core/shell octahedrons can be observed clearly, and the shell thickness is about 40 nm (Figure 7d inset). The corresponding energy dispersive spectroscopy (EDS) spectrum reveals the presence of elements of Mn, O, and C, and the calculated atomic ratio of Mn:O is about 0.95:1, indicating the presence of MnO and C rather than $MnCO_3$ in this core/shell sample. The HRTEM image taken from the broken area of a single octahedron (Figure 3e,f), further demonstrates the core is MnO and the shell is amorphous carbon in low graphitic level due to the relatively low carbonization temperature of 600 °C.

When other MOM samples are carbonized under the same conditions, similar MnO@C core/shell structures with an octahedron morphology can be obtained. It can be observed from the SEM and TEM images shown in Figure 8 that the sizes of the core/shell octahedrons increase with the particle sizes of the employed MOM samples, but the shell thickness of these obtained core/shell samples are little different (about 40 nm) under the same carbonization conditions. These results indicate that the size of the MnO@C core/shell octahedrons can be controlled by the used MOM sample, which can be tuned simply by varying the concentration of $Mn(Ac)_2$ in ethanol.

3.4. Characterization of Carbon Hollow Octahedrons (CHOs). On the basis of the above experimental results, it can be concluded that the MOMs can be used as raw materials for the fabrication of MnO@C core/shell octahedrons because their surfaces were encapsulated by the adsorbed oligomers,

which can be in situ carbonized on the surface of MOMs. After the removal of the inner MnO cores by HCl etching, the octahedron morphologies can be retained well and thus carbon hollow octahedrons (CHOs) can be formed.

Figure 9 shows the SEM and TEM images of the as-prepared CHOs by in situ carbonization of MOM-600 followed by HCl

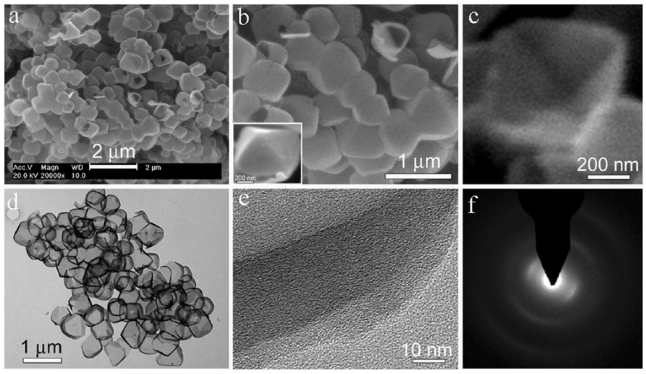

Figure 9. (a–c) SEM, (d) TEM, (e) HRTEM images, and (f) corresponding SAED pattern of the obtained CHOs using MOM-600 as starting material followed with HCl etching. Carbonization conditions: 600 °C, 6 h.

etching. As shown in Figure 9a, large-area carbon hollow octahedrons with a relatively uniform size were obtained. The enlarged SEM image in Figure 9b shows some broken octahedrons, suggesting the hollow structures of the sample. The top view in the inset of Figure 9b clearly illustrates the perfect octahedral shapes. Figure 9c presents the top view of one single hemi-octahedron, clearly depicting the octahedral shape of the hollow interior of CHOs, and the average edge length of the octahedron is about 600 nm. The TEM image in Figure 9d shows the general morphology of the CHOs with a thickness of about 30–50 nm and a cavity size of about 500–800 nm, which is slightly smaller than that of the core/shell structures owing to the structure shrinkage in the core removal process. The HRTEM image in Figure 9e and the corresponding SAED pattern in Figure 9f show the shell of CHOs is amorphous, which is consistent with the HRTEM observation in Figure 7e. These results indicate that the CHOs were from the in situ template effect of MnO octahedral mesocrystals, in which the in situ carbonization of the adsorbed oligomers resulted in the fabrication of MnO@C core/shell octahedrons.

As expected, the particle and cavity sizes of the carbon hollow octahedrons can be controlled by the sizes of the employed MOM template. The morphology observations of different CHO samples using different MOM templates can substantiate the above conclusion (Figure 10). The particle sizes of these CHO samples are about 600–850, 800–900, and 850–950 nm, when using MOM-600, MOM-750, and MOM-900 as in situ templates, respectively. It can also be seen that the cavity sizes of the CHOs are close to those of the MnO templates, and their shell thickness are similarly of about 40 nm, well consisting with the sizes of MnO@C core/shell octahedrons. These results suggest that the sizes of the CHOs can be controlled by the employed MnO octahedral mesocrystals, of which the sizes can be tuned by simply varying the concentration of $Mn(Ac)_2$ in ethanol. Owing to their novel morphology, large hollow interior, and controllable size, the synthesized CHOs may be of potential importance in various fields such as catalyst supports, microreactors, and energy storage, etc.

It should be noted that the oligomers absorbed on the surface of MOMs play a crucial role in the formation of a uniform carbon shell cover on the MOM surface. One of the direct evidences is that no CHOs with a well-defined shell could be obtained when the oligomers were removed by calcined under air atmosphere at 450 °C. As shown in Figure S5 (Supporting Information), a large number of carbon thin

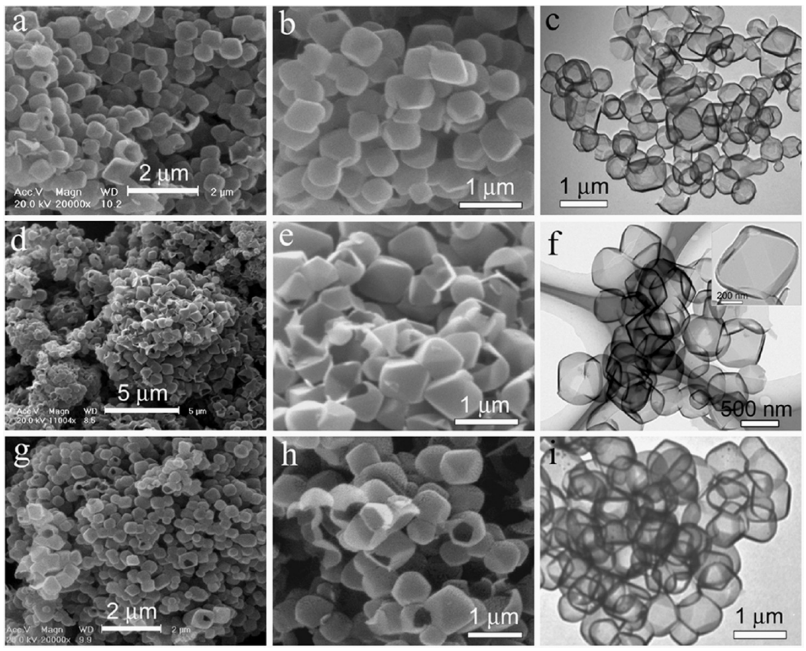

Figure 10. SEM and TEM images of the synthesized CHOs using different MOM samples as starting materials followed by HCl etching: (a–c) MOM-500, (d–f) MOM-750, and (g–i) MOM-900. Carbonization conditions: 600 °C, 6h.

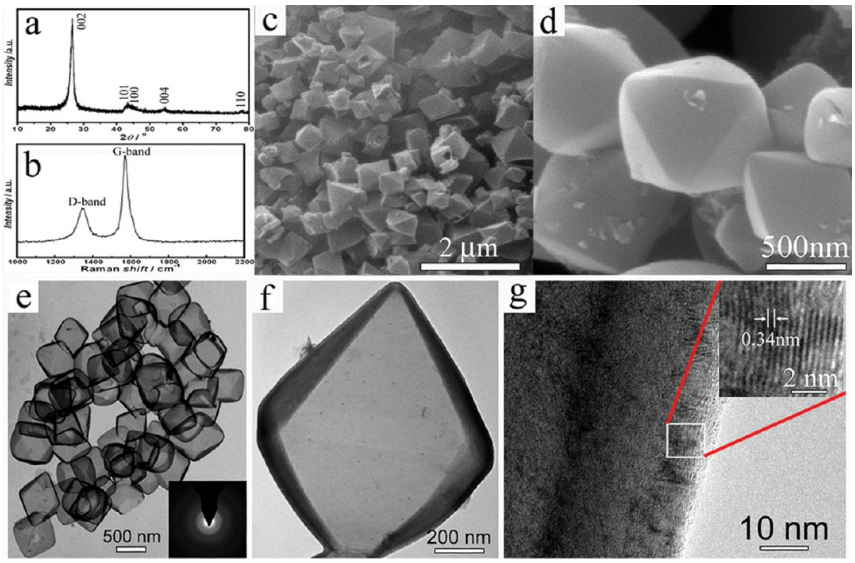

Figure 11. (a) XRD, (b) Raman spectrum, (c, d) SEM images, (e, f) TEM images, and (g) HRTEM image of the as-prepared HGOs using MOM-600 as a template.

sheets and few broken CHOs were obtained, indicating the nonuniform coating resulted in the inhomogeneous carbon shell when the oligomer shell was removed. In addition, the calcination time is another important factor to form a uniform carbon shell. In a short calcination time, a thin carbon shell was formed on the MOM surface, which also led to the formation of a large number of broken CHOs after HCl etching (Figure S6, Supporting Information). These results suggest that the absorbed oligomer layer and longer calcination time are important for the formation of uniform carbon shells and relatively perfect carbon hollow octahedrons.

3.5. Characterization of Graphitic Hollow Octahedrons (CHOs). Hollow graphitic carbons, including hollow spheres, nanocages, graphitic nanotubes, and capsules, have attracted growing attention owing to their promising applications in various fields of Li-ion batteries, catalyst supports, supercapacitors, and hydrogen storage.[65−68] Although polyhedral graphitic cages have been prepared previously,[69,70] the GHOs with high purities were difficult to obtain. In the present, a high purity of GHOs could be obtained by using MOMs as a template (MOM-600 as the example). The product was prepared by calcination in tubular furnace at a temperature of 900 °C followed by HCl etching. Figure 11a shows the typical XRD pattern of GHOs, in which four typical diffraction peaks: (002), (101), (100), (004), and (100), of graphite (JCPDS No. 75-1621) denote a high degree of graphitization of the GHOs. As shown in the Raman spectrum in Figure 11b, the intensity of the I_D/I_G ratio is ∼0.45, further indicating the high graphitization degree, which conforms with the XRD results.

The morphology of the resulting GHOs was examined by SEM and TEM. Bulk quantities of octahedrons with a relative particle size of 600−900 nm can be observed, as shown in Figure 11c. Figure 11d clearly illustrates the perfect octahedral shape, and the average edge length of HGOs is about 600−900 nm. Figure 11e displays the TEM image of HGOs with a uniform shell thickness of about 30−50 nm and an inner spacing of about 500−800 nm, consistent with the size of the employed template of MOM-600. From the SEM and TEM results, no other types of carbons could be seen, indicating the high purity of the as-prepared GHOs. The electron diffraction pattern is shown in the inset of Figure 11d. Figure11f presents a single octahedron with an edge length of 800−900 nm. From the HRTEM image in Figure 11g, graphitic carbon layers could be observed. The magnified HRTEM image (inset of Figure 11g) reveals a periodic fringe spacing of 0.34 nm corresponding to the interplanar spacing between the (200) planes of graphitic carbon, indicating the high degree of graphitization of GHOs, which is in good agreement with the XRD and Raman results.

4. CONCLUSIONS

In conclusion, manganese monoxide mesocrystals (MOMs) with uniform octahedron morphologies and controllable particle sizes have been successfully prepared by a simple additive-free method, in which manganese acetate and ethanol were used as raw materials. The selective adsorption of oligomers, resulted from the polymerization of ethanol, may play an important role in the mesocrystal formation process. A mechanism involving the oriented attachment of MnO NP subunits and subsequent ripening process is proposed. Remarkably, the as-prepared MnO octahedral mesocrystals were employed as in situ template to fabricate of MnO@C core/shells and carbon hollow octahedrons, in which the adsorbed oligomers acted as a carbon precursor for carbon shell formation. The particle sizes of MOMs, MnO@C core/shell octahedrons, and carbon hollow octahedrons can be tuned by simply varying the concentration of manganese acetate in ethanol. This novel strategy based on the oriented attachment and ripening mechanism will certainly open alternative doorways toward rational fabrication of various kinds of metal oxide mesocrystals, metal oxide@carbon core/shell materials, and carbon hollow structures with unique morphologies, controllable particle sizes, and large hollow interiors, which will shed new light on their novel applications and fundamental properties. Furthermore, in the present work, simple alcohol was used to direct the growth and aggregate that could lead to a better understanding of how organic species affect crystal growth, which is important in biomineralization and other materials sciences. This also shows the importance of mesocrystals not only for the field of material research but also for the application in functional materials synthesis.

■ ASSOCIATED CONTENT

Supporting Information

SEM images of the resulting MnO mesocrystals with different particle sizes, N_2 adsorption−desorption isotherms, and a pore size distribution curve of the sample MOM-500, and HRTEM images of the intermediate product are provided. This material is available free of charge via the Internet at http://pubs.acs.org.

■ AUTHOR INFORMATION

Corresponding Author

*Y. Liu. E-mail: tliuyl@163.com. Fax/Tel.: +86 20 85280323.

Author Contributions

The manuscript was written through contributions of all authors. All authors have given approval to the final version of the manuscript.

Notes

The authors declare no competing financial interest.

■ ACKNOWLEDGMENTS

The authors gratefully acknowledge the financial support from the National Natural Science Foundation of China (21031001 and 21201065), the Science and Technology Plan Projects of Guangdong Province (2011A081301018), the Key Program of the Science Technology Innovation Foundation of the Higher Education Institutions of Guangdong Province, China (cxzd1014), and the Minister Funds of South China Agricultural University.

■ REFERENCES

(1) Tian, Z. R.; Voigt, J. A.; Liu, J.; Mckenzie, B.; Mcdermott, M. J.; Rodriguez, M. A.; Konishi, H.; Xu, H. *Nat. Mater.* **2003**, *2*, 821−826.

(2) Tang, C.; Bombalski, L.; Kruk, M.; Jaroniec, M.; Matyjaszewski, K.; Kowalewski, T. *Adv. Mater.* **2008**, *20*, 1516−1522.

(3) Seo, M.; Hillmyer, M.A. *Science* **2012**, *336*, 1422−1425.

(4) Ali, I. *Chem. Rev.* **2012**, *112*, 5073−5091.

(5) Chen, J.; Yano, K. *ACS Appl. Mater. Inter.* **2013**, *5*, 7682−7687.

(6) Denis, G. *Angew. Chem., Int. Ed.* **2013**, *52*, 8208−8209.

(7) Liu, B.; Zeng, H. C. *J. Am. Chem. Soc.* **2004**, *126*, 8124−8125.

(8) Zhang, L. S.; Wang, W. Z.; Zhou, L.; Xu, H. L. *Small* **2007**, *3*, 1618−1625.

(9) Meldrum, F. C.; Cölfen, H. *Chem. Rev.* **2008**, *108*, 4332−4432.

(10) Chen, S. F.; Zhu, J. H.; Jiang, J.; Cai, G. B.; Yu, S. H. *Adv. Mater.* **2009**, *21*, 5853−5855.

(11) Chen, J. S.; Zhu, T.; Li, C. M.; Lou, X. W. *Angew. Chem., Int. Ed.* **2011**, *50*, 650−653.

(12) Simon, P.; Rosseeva, E.; Baburin, I. A.; Liebscher, L.; Hickey, S. G.; Cardoso-Gil, R.; Eychmuller, A.; Kniep, R.; Carrillo-Cabrera, W. *Angew. Chem., Int. Ed.* **2012**, *51*, 10776−10781.

(13) Cölfen, H.; Antonietti, M. *Angew. Chem., Int. Ed.* **2005**, *44*, 5576−5591.

(14) Rousseau, M.; Lopez, E.; Stempfle, P.; Brendle, M.; Franke, L.; Guette, A.; Naslain, R.; Bourrat, X. *Biomaterials* **2005**, *26*, 6254−6262.

(15) Liu, B.; Zeng, H. C. *Chem. Mater.* **2008**, *20*, 2711−2718.

(16) Zhou, L.; O'Brien, P. *Small* **2008**, *4*, 1566−1574.

(17) Song, R. Q.; Cölfen, H. *Adv. Mater.* **2010**, *22*, 1301−1330.

(18) Wu, X. L.; Xiong, S. J.; Liu, Z.; Chen, J.; Shen, J. C.; Li, T. H.; Wu, P. H.; Chu, P. K. *Nat. Nanotechnol.* **2011**, *6*, 103−106.

(19) Zhou, L.; O'Brien, P. *J. Phys. Chem. Lett.* **2012**, *3*, 620−628.

(20) Li, T.; You, H. J.; Xu, M. W.; Song, X. P.; Fang, J. X. *ACS Appl. Mater. Inter.* **2013**, *4*, 6941−6947.

(21) Xu, A. W.; Antonietti, M.; Cölfen, H.; Fang, Y. P. *Adv. Funct. Mater.* **2006**, *16*, 903−908.

(22) Xu, A. W.; Antonietti, M.; Yu, S. H.; Cölfen, H. *Adv. Mater.* **2009**, *20*, 1333−1338.

(23) Lenders, J. J. M.; Dey, A.; Bomans, P. H. H.; Spielmann, J.; Hendrix, M. M. R. M.; de With, G.; Meldrum, F. C.; Harder, S.; Sommerdijk, N. A. J. M. *J. Am. Chem. Soc.* **2012**, *134*, 1367−1373.

(24) Wang, T.; Mitchell, J.; Börner, H.; Cölfen, H.; Antonietti, M. *Phys. Chem. Chem. Phys.* **2010**, *12*, 11984−11992.

(25) Judat, B.; Kind, M. *J. Colloid Interface Sci.* **2004**, *269*, 341−350.

(26) Shevchenko, E. V.; Talapin, D. V.; Rogach, A. L.; Kornowski, A.; Haase, M.; Weller, H. *J. Am. Chem. Soc.* **2002**, *124*, 11480−11485.

(27) Jongen, N.; Bowen, P.; Lemaître, J.; Valmalette, J. C.; Hofmann, H. *J. Colloid Interf. Sci.* **2000**, *226*, 189−198.

(28) Gong, Q.; Qian, X.; Ma, X.; Zhu, Z. *Cryst. Growth Des.* **2006**, *6*, 1821−1825.

(29) Li, Z.; Geßner, A.; Richters, J.P.; Kalden, J.; Voss, T.; Kübel, C.; Taubert, A. *Adv. Mater.* **2008**, *20*, 1279−1285.

(30) Mo, M.S.; Lim, S.H.; Mai, Y.W.; Zheng, R.K.; Ringer, S. *Adv. Mater.* **2008**, *20*, 339−342.

(31) Tang, H.; Chang, J. C.; Shan, Y.; Lee, S.T. *J. Phys. Chem. B* **2008**, *112*, 4016−4021.

(32) Liu, S. J.; Gong, J. Y.; Hu, B.; Yu, S. H. *Cryst. Growth Des.* **2009**, *9*, 203−209.

(33) Hu, B.; Wu, L. H.; Liu, S. J.; Yao, H. B.; Shi, H. Y.; Li, G. P.; Yu, S. H. *Chem. Commun.* **2010**, *46*, 2277−2279.

(34) Lausser, C.; Cölfen, H.; Antonietti, M. *ACS Nano* **2011**, *5*, 107−114.

(35) Waltz, F.; Wißmann, G.; Lippke, J.; Schneider, A.M.; Schwarz, H. C. *Cryst. Growth Des.* **2012**, *12*, 3066−3075.

(36) Zhai, H. L.; Jiang, W.; Tao, J. H.; Lin, S. Y.; Chu, X. B.; Xu, X. R.; Tang, R. K. *Adv. Mater.* **2010**, *22*, 3729−3734.

(37) Geng, X.; Jiang, J.; Yu, S. H. *Crystal Growth Des.* **2010**, *10*, 3448−3453.

(38) Song, R. Q.; Cölfen, H.; Xu, A. W.; Hartmann, J.; Antonietti, M. *ACS Nano* **2009**, *3*, 1966−1978.

(39) Zhou, L.; Boyle, D. S.; O'Brien, P. *J. Am. Chem. Soc.* **2008**, *130*, 1309−1320.

(40) Zhou, L.; Wang, W.; Xu, H. *J. Phys. Chem. C* **2009**, *113*, 6584−6588.

(41) Zhan, H.; Yang, X.; Wang, C.; Chen, J.; Wen, Y.; Liang, C.; Greer, H. F.; Wu, M.; Zhou, W. *Cryst. Growth Des.* **2012**, *12*, 1247−1253.

(42) Liu, Y.; Zhang, Y.; Li, H.; Wang, J. *Cryst. Growth Des.* **2012**, *12*, 2625−2633.

(43) Wohlrab, S.; Pinna, N.; Antonietti, M.; Cölfen, H. *Chem.—Eur. J.* **2005**, *11*, 2903−2913.

(44) Chen, S. F.; Yu, S. H.; Wang, T. X.; Jiang, J.; Cölfen, H.; Hu, B. *Adv. Mater.* **2005**, *17*, 1461−1465.

(45) Ethirajan, A.; Ziener, U.; Landfester, K. *Chem. Mater.* **2009**, *21*, 2218−2225.

(46) Distaso, M.; Taylor, R. N. K.; Taccardi, N.; Wasserscheid, P.; Peukert, W. *Chem.—Eur. J.* **2011**, *17*, 2923−2930.

(47) Nassif, N.; Gehrke, N.; Pinna, N.; Shirshova, N.; Taue, K.; Antonietti, M.; Cölfen, H. *Angew. Chem., Int. Ed.* **2005**, *44*, 6004−6009.

(48) Yu, S. H.; Cölfen, H.; Tauer, K.; Antonietti, M. *Nat. Mater.* **2005**, *4*, 51−55.

(49) Wang, T.; Xu, A. W.; Cölfen, H. *Angew. Chem., Int. Ed.* **2006**, *45*, 4451−4455.

(50) Sun, Z. W.; An, Q. F.; Zhao, Q.; Shangguan, Y. G.; Zheng, Q. *Cryst. Growth Des.* **2012**, *12*, 2382−2388.

(51) Zhou, L.; Wang, W.; Xu, H. *Cryst. Growth Des.* **2008**, *8*, 728−733.

(52) Ye, J. F.; Liu, W.; Cai, J. G.; Chen, S.; Zhao, X. W.; Zhou, H. H.; Qi, L. M. *J. Am. Chem. Soc.* **2011**, *133*, 933−940.

(53) Zheng, M.; Liu, Y.; Zhao, S.; He, W.; Xiao, Y.; Yuan, D. *Inorg. Chem.* **2010**, *49*, 8674−8673.

(54) Yu, S. H.; Chen, S. *Curr. Nanosci.* **2006**, *2*, 81−92.

(55) Niederberger, M.; Cölfen, H. *Phys. Chem. Chem. Phys.* **2006**, *8*, 3271−3287.

(56) Vazquez-Olmos, A.; Redon, R.; Rodriguez-Gattorno, G.; Mata-Zamora, M. E.; Morales-Leal, F.; Fernandez-Osorio, A. L.; Saniger, J. M. *J. Colloid Interface Sci.* **2005**, *291*, 175−180.
(57) Liang, S.; Teng, F.; Bulgan, G.; Zong, R.; Zhu, Y. *J. Phys. Chem. C* **2008**, *112*, 5307−5315.
(58) Chen, H.; He, J. *J. Phys. Chem. C* **2008**, *112*, 17540−17545.
(59) Penn, R. L.; Banfield, J. F. *Science* **1998**, *281*, 969−971.
(60) Lu, W. G.; Fang, J. Y. *J. Phys. Chem. B* **2005**, *109*, 19219−19222.
(61) Liang, X.; Gao, L.; Yang, S.; Sun, J. *Adv. Mater.* **2009**, *21*, 2068−2071.
(62) Hoshino, A.; Fujioka, K.; Oku, T.; Suga, M.; Sasaki, Y. F.; Ohta, T.; Yasuhara, M.; Suzuki, K.; Yamamoto, K. *Nano Lett.* **2004**, *4*, 2163−2169.
(63) Yin, H.; Too, H. P.; Chow, G. M. *Biomaterials* **2005**, *26*, 5818−5826.
(64) Imai, H.; Tochimoto, N.; Nishino, Y.; Takezawa, Y.; Oaki, Y. *Cryst. Growth Des.* **2012**, *12*, 876−882.
(65) Chen, Y. M.; Lu, Z. G.; Zhou, L. M.; Mai, Y. W.; Huang, H. T. *Energy Environ. Sci.* **2012**, *5*, 7898−7902.
(66) Schaefer, Z. L.; Gross, M. L.; Hickner, M. A.; Schaak, R. E. *Angew. Chem., Int. Ed.* **2010**, *49*, 7045−7048.
(67) Ma, F. W.; Zhao, H.; Sun, L. P.; Li, Q.; Huo, L. H.; Xia, T.; Guo, S.; Pang, G. S.; Shi, Z.; Feng, S. H. *J. Mater. Chem.* **2012**, *22*, 13464−13468.
(68) Yang, S. J.; Cho, J. H.; Oh, G. H.; Nahm, K. S.; Park, C. R. *Carbon* **2009**, *47*, 1585−1591.
(69) Li, H. B.; Yue, Q. L.; Xu, S. L.; Wang, L.; Liu, J. F. *Mater. Lett.* **2012**, *66*, 353−356.
(70) Mei, T.; Li, N.; Li, Q. W.; Xing, Z.; Tang, K. B.; Zhu, Y. C.; Qian, Y. T.; Shen, X. Y. *Mater. Res. Bull.* **2012**, *4*, 1604−1608.